processes

MDPI

Article

Regulatory Mechanisms of Particle Dynamics and Deposition Distribution in Bend Pipes with Curvature Ratio

Tianyu Gong [1], Youhang Zhou [1,*], Xuan Tang [1], Zhenhai Liu [1], Ding Li [1] and Yuqin Xiao [2,*]

[1] School of Mechanical Engineering and Mechanics, Xiangtan University, Xiangtan 411105, China; 202231570221@smail.xtu.edu.cn (T.G.); tangxuan@xtu.edu.cn (X.T.); 202431640353@smail.xtu.edu.cn (Z.L.); m19386690214@163.com (D.L.)

[2] Department of Engineering Education, Xiangtan University, Xiangtan 411105, China

* Correspondence: zhouyouhang@xtu.edu.cn (Y.Z.); xiaoyuqin@xtu.edu.cn (Y.X.); Tel.: +86-133-3722-9129 (Y.Z.); +86-153-7739-1030 (Y.X.)

Abstract

Curvature ratio (δ) governs secondary flows in gas–solid two-phase flow through bends, thereby affecting particle dynamics and leading to non-uniform wall deposition and increased erosion risk. In this study, a coupled Reynolds stress model (RSM) and Discrete phase model (DPM) framework was employed. A wall contact model incorporating adhesion, rebound, and removal mechanisms was implemented via a User-Defined Function (UDF). The spatial distribution and deposition characteristics of particles with different inertia (Stokes number range: $0.020 \leq St \leq 30.176$) were systematically investigated in the range of δ = 2.0~3.5. The results reveal a distinct inertial dependence in particle spatial distribution: particles with $St < 1$ exhibit a "high-dispersion, weak-aggregation" pattern, whereas those with $St > 1$ form an "outer-wall agglomeration, inner-wall cavity" characteristic. As δ increases, the secondary flow intensity decreases while the effective centrifugal path lengthens. Governed by the combined effects of the effective collision coefficient (Rc) and effective adhesion rate (η_a), particle deposition is inhibited for $St < 1$ but enhanced for $St > 1$. This study advances the understanding of deposition under geometric constraints and provides a basis for optimizing pipeline design.

Keywords: gas-solid two-phase flow; curvature ratio; particle deposition; numerical simulation

1. Introduction

Pneumatic conveying, an efficient method for transporting particulate materials, has been widely adopted in industrial sectors such as mining, food processing, and energy [1,2]. During the conveying process, the particulate phase is subject to the combined effects of gas-phase turbulence, interparticle interactions, and wall constraints, exhibiting significant randomness and complexity [3]. As a crucial component in altering the conveying direction, the flow characteristics of gas–solid two-phase flow within a bend significantly influence the system's overall operational efficiency and stability. Specifically, the centrifugal forces, secondary flows, and reverse pressure gradients induced by sudden changes in flow direction not only alter particle trajectories [4] but also tend to cause non-uniform particle deposition in specific wall regions [5]. Consequently, this results in increased energy consumption, reduced conveying efficiency, and issues such as pipeline blockages and wall erosion [6,7]. Therefore, a thorough elucidation of the mechanisms governing particle

Academic Editors: Vivek Garg and Jan Nečas

Received: 1 March 2026
Revised: 2 April 2026
Accepted: 11 April 2026
Published: 15 April 2026

transport and deposition within bends is of great significance for the optimized design of pneumatic conveying systems.

Among the geometric parameters affecting gas–solid flow in bend pipes, the curvature ratio is a key factor regulating the flow field structure and particle motion behavior. Increasing the curvature ratio slows the rate of pressure gradient decay and reduces system pressure drop [8,9]. It also increases particle exit velocity and delays velocity decay, thus reducing operational energy consumption [10,11]. Conversely, an excessively small curvature ratio exacerbates wall erosion due to changes in particle-wall collision frequency and impact angles [6]. Studies by Benyamine et al. [12] and Shao et al. [13] confirm that reducing the curvature ratio intensifies the propensity of particles to impact the wall. This significantly affects the total deposition mass and spatial distribution. These macroscopic phenomena relate closely to the evolution of secondary flow induced by the pipe's curvature. Since the experimental observations by Eustice [14] and the theoretical analysis by Dean [15], the influence of secondary flow on the velocity distribution of the main flow and flow stability has been widely recognized [16]. Kim et al. [17] further indicated that the vorticity intensity of the secondary flow is mainly controlled by the curvature ratio, showing weak correlation with the Reynolds number. Changes in the curvature ratio affect the intensity, location, and scale of the secondary flow. They also determine the spatial distribution patterns of the gas–solid two-phase flow within the bend pipe.

In recent years, researchers have increasingly recognized that the curvature ratio not only influences the distribution of the gas-phase flow field. It also profoundly affects particle transport and deposition behavior by regulating the secondary flow structure. Inthavong [18] conducted a visualization analysis of the flow within the vortex core. They revealed the relative intensity of secondary flows, finding that sufficiently strong secondary flows can carry particles from the outer wall to the inner wall. Lira et al. [19] pointed out that secondary flows are the primary mechanism for particle centrifugation, while the influence of counter-rotating vortices is relatively minor and leads to a decrease in local particle concentration. Li et al. [20] found that secondary flows expand the contact area between particles and the wall, as well as the deposition zone. Increasing the curvature ratio can effectively reduce the deposition zone. Sun et al. [21] observed that secondary flows and streamwise vortices enhance the transport of small particles toward the wall. Crucially, Yan et al. [22] revealed the coupling effect between centrifugal force and secondary flow. Centrifugal force drives high-inertia particles toward the outer wall, forming a "reflection layer", while secondary flow transports some low-inertia particles to the inner wall region. Collectively, these studies indicate that the curvature ratio, as a key parameter regulating the evolution of secondary flow, interacts with centrifugal force through a complex coupling mechanism to jointly regulate particle transport and deposition behavior.

In addition to the flow field structure, particle inertia, characterized by the Stokes number, determines their response to the flow field structure, resulting in distinctly different deposition patterns for particles of different sizes. Yang et al. [23] found that particles converge at bends and form "particle ropes" under the influence of inertia. Berrouk et al. [24] reported that high-inertia particles primarily deposit on the outer wall of the curved pipe, while low-inertia particles are distributed between the side walls and inner wall. The non-depositional region on the inner wall is caused by small-scale vortices dominated by secondary flow. Subsequent studies further validated this inertia-dominated deposition pattern. Jiang et al. [25] and Vasquez et al. [26] observed that high-inertia particles, due to inertial impact, concentrate and deposit on the middle and downstream sections of the outer wall. Guo et al. [27] found that the primary deposition location of particles is closely related to the Stokes number. Deposition efficiency on the inner wall increases, then decreases, as *St* increases. These studies established that the inertial effect is one of the primary controlling mechanisms of particle deposition.

In summary, existing studies have separately examined the effects of curvature ratio, secondary flow evolution, and particle inertia on deposition behavior. However, a systematic understanding remains lacking of how the coupled interaction between secondary flow intensity and centrifugal force governs particle transport and deposition across different curvature ratios. Specifically, it remains unclear how variations in curvature ratio modulate the secondary flow vortex structures and centrifugal force, thereby influencing particle transport mechanisms and ultimately determining the deposition distribution on the inner and outer walls. Addressing this theoretical gap is essential for advancing the optimization design of pneumatic conveying systems in bend pipes based on curvature ratio control.

In numerical simulations, researchers have continuously optimized the accuracy of models to capture the aforementioned complex coupling mechanisms. As demonstrated by related studies, the Reynolds Stress Model (RSM) has been shown to outperform traditional models in capturing anisotropic turbulence and secondary flow structures [28]. Furthermore, combining the RSM with the Enhanced Wall Treatment (EWT) method has been demonstrated to effectively improve the accuracy of near-wall simulations [29,30]. In addition, contact models based on particle-wall collisions provide more accurate descriptions of the rebound and resuspension behavior of large particles than the traditional "trap" model [31]. The development of these numerical methods has provided reliable tools for elucidating the mechanisms by which curvature ratio influences particle transport and deposition.

To this end, this study established a numerical framework that couples the Reynolds Stress Model (RSM) with the Discrete Phase Model (DPM) and employs a User-Defined Function (UDF) to accurately characterize particle-wall interactions. On this basis, the evolution characteristics of secondary flow in bend pipes with varying curvature ratios are systematically analyzed. The quantitative effects of secondary flow and centrifugal force on the transport behavior and deposition distribution of particles with different inertia are assessed. The objective of this study is to elucidate the underlying mechanisms linking "curvature ratio—secondary flow evolution—particle inertial response—deposition distribution." This theoretical framework provides a foundation for predicting particle transport and deposition in bend pipes under complex geometric constraints.

2. Materials and Methods

2.1. Model Configuration

This study investigates the pneumatic conveying bend integrated into the sepiolite particle classification system. As illustrated in Figure 1, the pipe has an inner diameter D = 20 mm, with an inlet section of $H = 10D$ and an outlet section of $L = 5D$. The curvature radius R_b = 40, 50, 60, and 70 mm, with corresponding curvature ratios $\delta = R_b/D$ of 2.0, 2.5, 3.0, and 3.5, respectively.

2.2. Gas Phase Turbulence Model

In this study, the gas phase is assumed to be a continuous and incompressible fluid. The RSM is employed to resolve the gas-phase turbulence. The continuity, momentum conservation, and Reynolds stress transport equations have been thoroughly described in Refs. [20,30] and are not reiterated here.

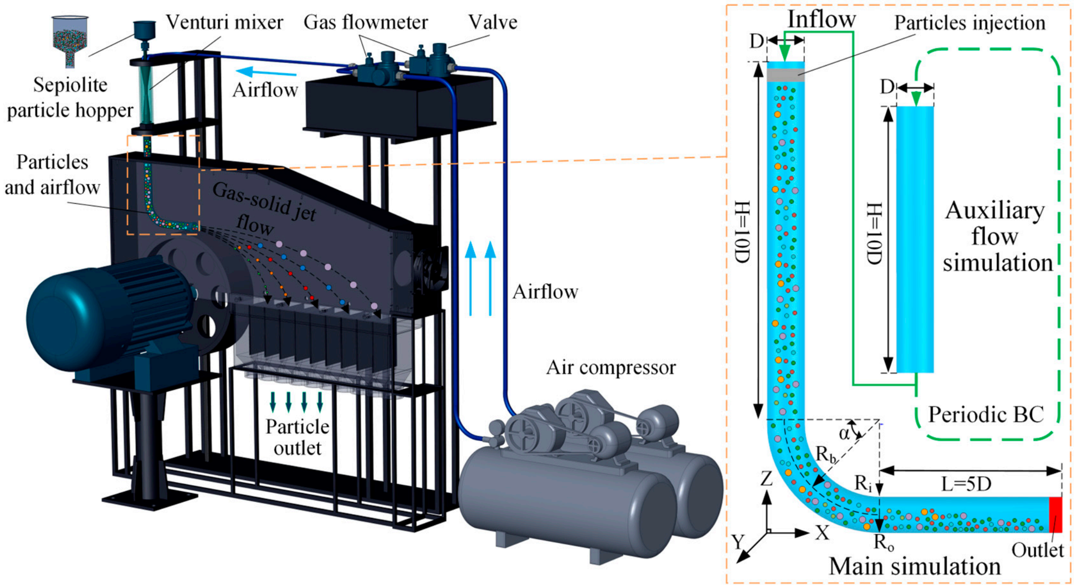

Figure 1. Structural parameters of pneumatic conveying bends.

The near-wall treatment employs the Enhanced Wall Treatment (EWT), which combines a two-layer zonal model with enhanced wall functions. The viscous-affected near-wall region ($Re_y < 200$) is resolved with Wolfshtein's one-equation model [32], while the fully turbulent region ($Re_y > 200$) is governed by the RSM transport equations. The wall Reynolds number Re_y is defined as follows:

$$Re_y = \frac{y\sqrt{k}}{v}. \tag{1}$$

The turbulent dissipation rate ε and dynamic viscosity μ_t are computed as follows:

$$\varepsilon = \frac{k^{3/2}}{l_\varepsilon}, \tag{2}$$

$$\mu_t = \rho C_\mu l_\mu \sqrt{k}. \tag{3}$$

where l_μ represents the momentum transport length scale, characterizing the effective range of turbulent momentum diffusion in the wall-normal direction, and l_ε denotes the energy dissipation length scale, representing the characteristic length associated with the transfer of turbulent kinetic energy from large-scale, energy-containing eddies to small-scale dissipative eddies. The specific mathematical definitions are as follows:

$$l_\mu = yC_l\left(1 - e^{-(Re_y/A_\mu)}\right), \tag{4}$$

$$l_\varepsilon = yC_l\left(1 - e^{-(Re_y/A_\varepsilon)}\right). \tag{5}$$

where $C_l = \kappa C_\mu^{-3/4}$ (κ = 0.4187 is the von Kármán constant), $C_\mu = 0.09$, $A_\mu = 70$ and $A_\varepsilon = 2C_l$.

2.3. Particle Phase Motion Model

The DPM is employed to track particle motion. Since the particle-to-gas volume fraction in the computational domain is 0.08%, well below 5%, interphase interactions and inter-particle collisions are neglected [33]. The discrete phase consists of sepiolite particles with a density ratio to the fluid of 1420.41. Therefore, minor forces such as the pressure gradient, Basset, and virtual mass forces are disregarded. All particles are treated as nonrotating solid spheres, so the Magnus force is also neglected [34]. The motion equation for the particle phase is as follows:

$$m_p \frac{du_p}{dt} = m_p g\left(1 - \frac{\rho}{\rho_p}\right) + F_D + F_S + F_B. \tag{6}$$

where m_p is the particle mass; g is the gravitational acceleration; u_p is the particle velocity vector; ρ and ρ_p are the fluid and particle densities, respectively. The drag force (F_{D}), Saffman lift force (F_S), and Brownian force (F_B) are defined as follows:

$$F_{\mathrm{D}} = m_p \frac{3\mu C_D Re_p}{4\rho_p d_p^2}. \tag{7}$$

where μ is the dynamic viscosity d_p is the particle diameter, C_D is the drag coefficient of momentum transfer for fluid and particle, Re_p is the Particle Reynolds number.

$$C_D = \begin{cases} \dfrac{24}{Re_p}, & Re_p < 1 \\ \dfrac{24}{Re_p}\left(1 + 0.15{Re_p}^{0.687}\right), & 1 < Re_p < 400 \end{cases} \tag{8}$$

$$Re_p = \frac{\rho d_p \left|u - u_p\right|}{\mu}. \tag{9}$$

where u is the fluid velocity. F_S and F_B are defined as follows:

$$F_S = m_p \frac{2\rho K_c v^{1/2}}{\rho_p d_p (S_{lk} S_{kl})^{1/4}} S_{ij} (u - u_p), \tag{10}$$

$$F_B = m_p \zeta \sqrt{\frac{\pi S_0}{\Delta t}}, \tag{11}$$

$$S_0 = \frac{216 v T k_b}{\pi^2 \rho_p d_p^5 S C_c}. \tag{12}$$

where $K_c = 2.594$ is the constant coefficient of Saffman lift force; S_{ij} is the mean strain-rate tensor; $\zeta \sim N(0,1)$ is the independent Gaussian white noise; T is the absolute temperature of the fluid; $k_b = 1.38 \times 10^{-23}$ J/K is the Boltzmann constant; S is the particle-to-fluid density ratio; and C_c is the Cunningham correction factor, defined as follows:

$$C_C = 1 + \frac{2\lambda}{d_p}\left(1.257 + 0.4e^{-\left(\frac{1.1 d_p}{2\lambda}\right)}\right). \tag{13}$$

where λ = 0.065 μm is the free path of gas molecules.

The effect of turbulence on particle motion is analyzed by the Discrete Random Walk (DRW) model. This method enables accurate quantification of the effects of turbulent fluctuations on particle diffusion and deposition [29]. Combining the RSM with DRW provides an effective approach for investigating particle deposition [30,34]. The turbulent fluctuation velocity is defined as follows:

$$u_i' = \zeta \sqrt{\overline{u_i'^2}}, \tag{14}$$

where $\sqrt{u_i'^2}$ is the root mean square (RMS) of the i-th velocity fluctuation. The turbulent eddy and integration time scales are defined as follows:

$$\tau_e = 2T_L, \tag{15}$$

$$T_L \approx 0.30\frac{k}{\varepsilon}. \tag{16}$$

2.4. Particle-Wall Interaction Model

Based on the critical deposition velocity theory of Brach et al. [35], a model for determining the contact state between particles and the pipe wall was constructed in this study. It is characterized by two states: wall rebound and adhesion deposition, as shown in Figure 2. The determination of contact states is defined as follows:

$$P_{state} = \begin{cases} 0, & |v_{pn}| > v_{cr} \\ 1, & |v_{pn}| \leq v_{cr} \end{cases} \tag{17}$$

where P_{state} denotes the contact state. v_{pn} is the normal impact velocity component of the particle. v_{cr} is the critical deposition velocity. Deposition occurs when $|v_{pn}| \leq v_{cr}$; otherwise, the particle rebounds. The v_{cr} is defined as follows:

$$v_{cr} = \left[\frac{2E}{d_p R^2}\right]^{\frac{10}{7}}. \tag{18}$$

where the particle restitution coefficient R = 0.9 [36]. The effective stiffness E is calculated as follows:

$$E = 0.51\left[\frac{5\pi^2(k_s + k_p)}{4\rho_p{}^{3/2}}\right]^{\frac{2}{5}}, \tag{19}$$

$$k_s = \frac{1-\nu_s^2}{\pi E_s}, \tag{20}$$

$$k_p = \frac{1-\nu_p^2}{\pi E_p}. \tag{21}$$

where E_s and E_p are the equivalent Young's modulus for the wall and particle, respectively. ν_s and ν_p denote the corresponding Poisson ratios.

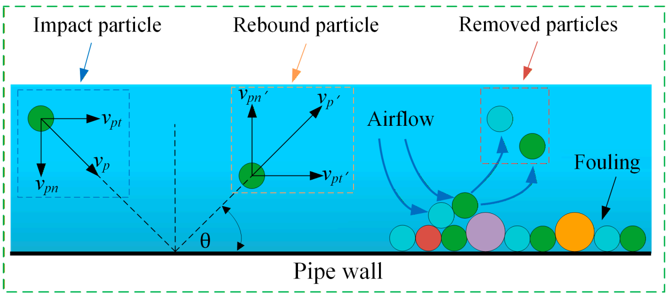

Figure 2. The schematic of particle-wall interaction.

The evolution of particle deposition is regulated by the interplay between adhesion and removal mechanisms, and this phenomenon is particularly significant in high-velocity flow regions [37]. Based on the JKR adhesion theory, Soltani et al. [38] proposed the critical shear velocity ($v_{\tau,\mathrm{crit}}$) required for particle detachment from the wall, a result that has been confirmed in subsequent research [39].

$$v_{\tau,crit} = 0.46\left(\frac{C_c^{3/2} W_A^2 \pi^{1/2}}{\rho^{3/2} {d_p}^2 K^{1/2}}\right)^{\frac{1}{3}}, \tag{22}$$

$$K = \frac{4}{3}\left[\frac{1-\nu_s^2}{E_s} + \frac{1-\nu_p^2}{E_p}\right]^{-1}, \tag{23}$$

$$\tau_{w,crit} = {v_{\tau,crit}}^2 \rho. \tag{24}$$

where W_A is the adhesion work, K is the composite Young's modulus, $\tau_{w,crit}$ is the critical wall shear stress. When the wall shear stress $\tau_w > \tau_{w,crit}$, adhered particles will be detached by the fluid.

In bend pipe flow, centrifugal forces significantly enhance the tendency of particles to impact the wall. This study employs the Grant–Tabakoff rebound model to describe the energy loss and velocity variation in particles after impacting the wall:

$$\begin{cases} e_n = \frac{v_{pn}\prime}{v_{pn}} = 0.993 - 1.76\theta + 1.56\theta^2 - 0.49\theta^3 \\ e_t = \frac{v_{pt}\prime}{v_{pt}} = 0.988 - 1.66\theta + 2.11\theta^2 - 0.67\theta^3 \end{cases} \tag{25}$$

where θ denotes impact angle, e_n and e_t represent normal and tangential restitution coefficients, respectively; v_{pt} represents tangential components of particle impact velocity. The superscript "′" denotes a rebound variable.

2.5. Particle Deposition Characteristic Parameters

The deposition characteristics of particles are characterized by St, the deposition velocity (V_d), and the dimensionless deposition velocity (V_d^+) [33,34]. St is defined as the ratio of the particle relaxation time (τ_p) to system response time (τ_s).

$$St = \frac{\tau_p}{\tau_s} = \frac{SC_c {d_p}^2 u_m}{9vD}, \tag{26}$$

$$V_d = -\frac{Du_m ln\left(1 - \frac{N_{dep}}{N_{in}}\right)}{Lc}, \tag{27}$$

$$V_d^+ = \frac{V_d}{u^*} = \frac{V_d}{\sqrt{\tau_w/\rho}}. \tag{28}$$

where u_m is the mean flow velocity, Lc is the computational domain length, N_{dep} and N_{in} are the numbers of deposited and released particles, respectively, u^* is the wall frictional velocity, τ_w is the wall shear stress. The Reynolds number is defined as follows:

$$Re = \frac{Du_m}{v}, \tag{29}$$

The effective adhesion rate η_a and the effective collision coefficient Rc of the particle are defined as follows:

$$\eta_a = \frac{N_{dep}}{N_c} \times 100\%, \tag{30}$$

$$Rc = \frac{N_c}{N_{in}}. \tag{31}$$

where N_c is the contact frequency between the particle and the wall.

3. Boundary Conditions and Model Validation

3.1. Numerical Method and Boundary Conditions

The numerical framework was established in ANSYS Fluent 2021R1, which solves the fluid governing equations via the finite volume method. The particle-wall interaction model was implemented by UDF (DEFINE_DPM_BC macro). Pressure-velocity coupling was handled through the SIMPLEC algorithm. Spatial discretization employed a second-order scheme for pressure, a second-order upwind scheme for convection, and a central difference scheme for diffusion. Solution convergence was considered achieved when residuals fell below 1×10^{-5} and the monitored variables stabilized within a 1% variation.

To establish fully developed turbulent inlet conditions, an auxiliary simulation was conducted in a straight pipe section spanning 10 diameters [40], with a gas velocity of 8m/s, as shown in Figure 1. Periodic boundary conditions were applied at the inlet and outlet of this auxiliary domain, with the mass flow rate maintained constant by dynamically adjusting the streamwise pressure gradient. After the flow reached a fully developed state, the flow field data at the outlet plane were extracted and imposed as the inlet boundary condition for the main simulation [41].

In the main simulation, the pipe wall was assigned a no-slip condition, and a pressure-outlet condition was specified at the outlet. The wall material was polymethyl methacrylate (PMMA), with sepiolite particles constituting the dispersed phase. Due to their high specific surface area and surface energy, sepiolite particles exhibit a strong propensity for adhesion and deposition on pipe walls during pneumatic conveying. Particle size distribution was measured using a LAP-W800H laser particle size analyzer, and the contact angle parameters were obtained using a DSAS100 contact angle testing system to calculate particle surface energy. The corresponding results are presented in Figure 3, with the key physical parameters summarized in Table 1.

Table 1. Material physical parameters.

Physical Parameters	Value
Gas temperature T/(k)	298.15
Gas density ρ/(kg/m^3)	1.225
Dynamic viscosity μ/(kg/m·s)	1.789×10^{-5}
Particle density ρ_p/(kg/m^3)	1740
Wall density ρ_s/(kg/m^3)	1160
Poisson ratio of particles ν_p	0.2
Poisson ratio of wall ν_s	0.375
Young's modulus of particles E_p/(GPa)	1.106
Wall Young's modulus E_s/(GPa)	2.75
Volumetric specific surface area/(cm^2/cm^3)	31,124.56
Adhesion work W_A/(J/m^2)	0.0523

To cover the primary range of the actual particle size distribution, seven characteristic particle sizes (n = 7) were selected at equal intervals from δ_{min} = 5% to δ_{max} = 95% based on the cumulative volume distribution: 3.0 μm, 7.0 μm, 12.0 μm, 18.0 μm, 26.0 μm, 40.0 μm, and 65.0 μm. The specific selection method is as follows:

$$\delta_i = \delta_{min} + \frac{i-1}{n-1}(\delta_{max} - \delta_{min}) \ \ (i \in N^*). \tag{32}$$

After the flow field converged, 10,000 spherical particles were uniformly released at a circular cross-section located 10 mm downstream from the inlet. Statistical verification confirmed that releasing more than 1000 particles can ensure stable statistical results [42].

The initial velocity of particles was set to the local mean fluid velocity at the injection position. Particles exiting the outlet were regarded as "escaped" and excluded from subsequent calculations.

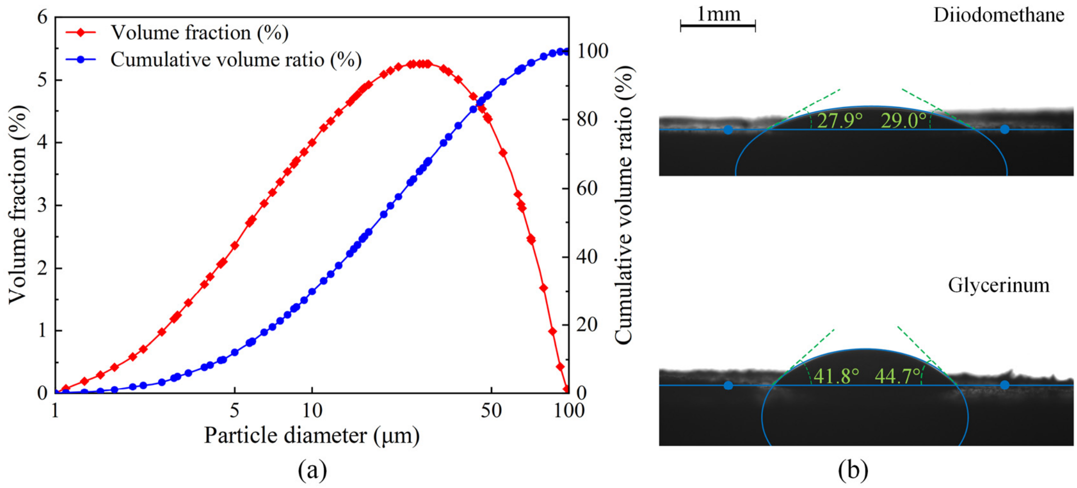

Figure 3. (**a**) Particle size distribution of sepiolite particles; (**b**) Contact angle of sepiolite particles.

3.2. Grid Independence Analysis and Numerical Model Verification

The computational domain was discretized using a structured grid, with local refinement applied in the bend and near-wall regions, as shown in Figure 4a. Four mesh schemes were selected for grid independence verification, with the mean gas velocity and mean pressure on five cross-sections in the bend region as the evaluation indicators. The corresponding grid information and pressure drop are presented in Table 2.

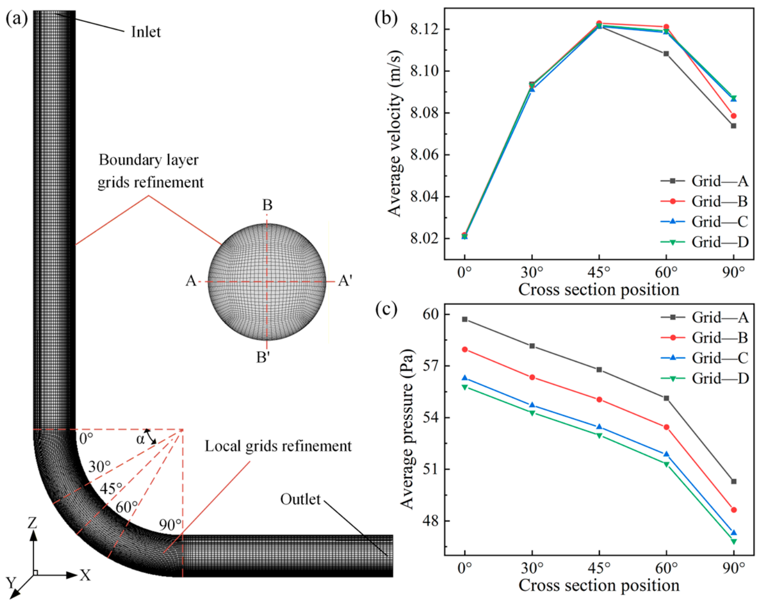

Figure 4. (**a**) Grid model; (**b**) Mean gas velocity at cross-section; (**c**) Mean pressure at cross-section.

As shown in Figure 4b,c, the pressure drop deviation between Schemes C and D was less than 1.5%, and the mean velocity and pressure distributions at all monitored locations were nearly identical. Considering both computational cost and accuracy, Scheme C was selected as the standard for subsequent mesh generation: 16 boundary-layer layers, a first-layer height of 0.03 mm, and a normal growth rate of 1.15.

Table 2. Grid division scheme in grid independence verification.

Scheme	Cells	Nodes	Number of Cross-Sectional Grids	Pressure Drop (Pa)
A	219648	212457	1024	34.886
B	406240	394933	1520	33.187
C	694692	677888	2001	31.508
D	969904	949455	2652	31.233

To assess the accuracy of the numerical model, the dimensionless fluctuation velocity $u'^{+}_{i,rms} = \sqrt{\overline{u'^{2}_{i}}}/u^{*}$ was compared in the fully developed region, as shown in Figure 5a. The simulated results agree well with the data reported by Yan et al. [41] and Wu et al. [43], with a maximum deviation of 7.06%, primarily attributable to differences in Reynolds number. Further validation was conducted by comparing the dimensionless mean streamwise velocity u_s/u_m (where u_s is the streamwise velocity) at various cross-sections, as presented in Figure 5b. The position is normalized by the dimensionless center wall distance $r^{*} = (r - r_i)/(r_o - r_i)$. The predicted u_s/u_m values are in excellent agreement with the numerical results of Yan et al. [41] and follow the trend of the experimental data of Sudo et al. [44]. Although observable deviations exist in the near-wall region. These discrepancies are mainly due to the resolution limitations inherent in early experimental measurements and are considered systematic errors within an engineering acceptable range. This indicates the reliability of the present model in capturing turbulent flow structures.

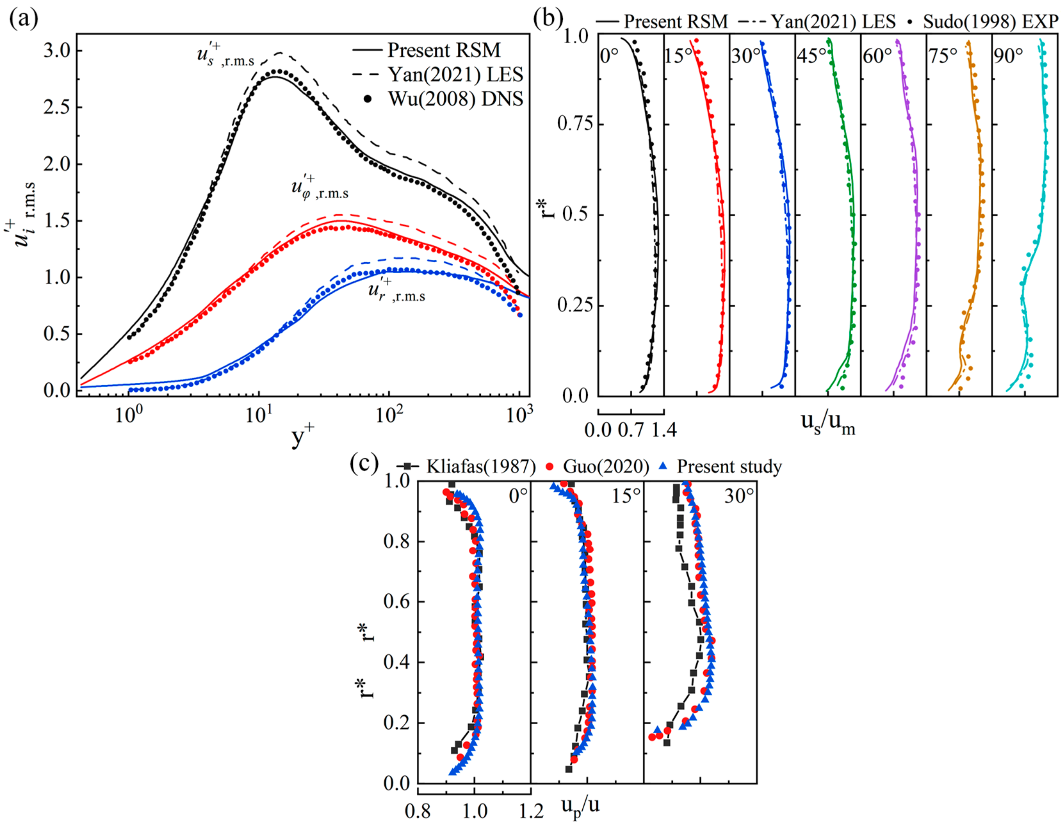

Figure 5. Gas-phase velocity and particle-phase velocity verification: (**a**) Gas-phase velocity: $u'^{+}_{i,rms}$ and y+ (Yan (2021) [41], Wu (2008) [43]); (**b**) Gas-phase velocity: (u_s/u_m) and r^{*} (Yan (2021) [41], Sudo (1998) [44]); (**c**) Particle-phase velocity: (u_p/u_m) and r^{*} (Kliafas (1987) [45], Guo (2020) [27]).

Validation was further extended to the dimensionless particle velocity u_p/u_m at cross-sections of $\alpha = 0°$, 15° and 30°, using the experimental parameters of Kliafas et al. [45]. As illustrated in Figure 5c, the predicted results agree well with previous studies. Although a noticeable deviation from the experimental values is observed at α = 30°, the results are consistent with the data in Ref. [27]. This agreement further confirms the reliability and accuracy of the present numerical approach and computational model.

4. Results and Discussion

4.1. Flow Field Characteristic Analysis

Figure 6 presents the distributions of flow velocity and velocity vectors at various deflection angles for $\delta = 2.0$. Upstream of the bend, at $\Delta Z/D = 1$, the mainstream velocity is oriented perpendicular to the pipe cross-section, with the maximum velocity located at the geometric center. This yields a centrosymmetric contour pattern characteristic of fully developed turbulent flow.

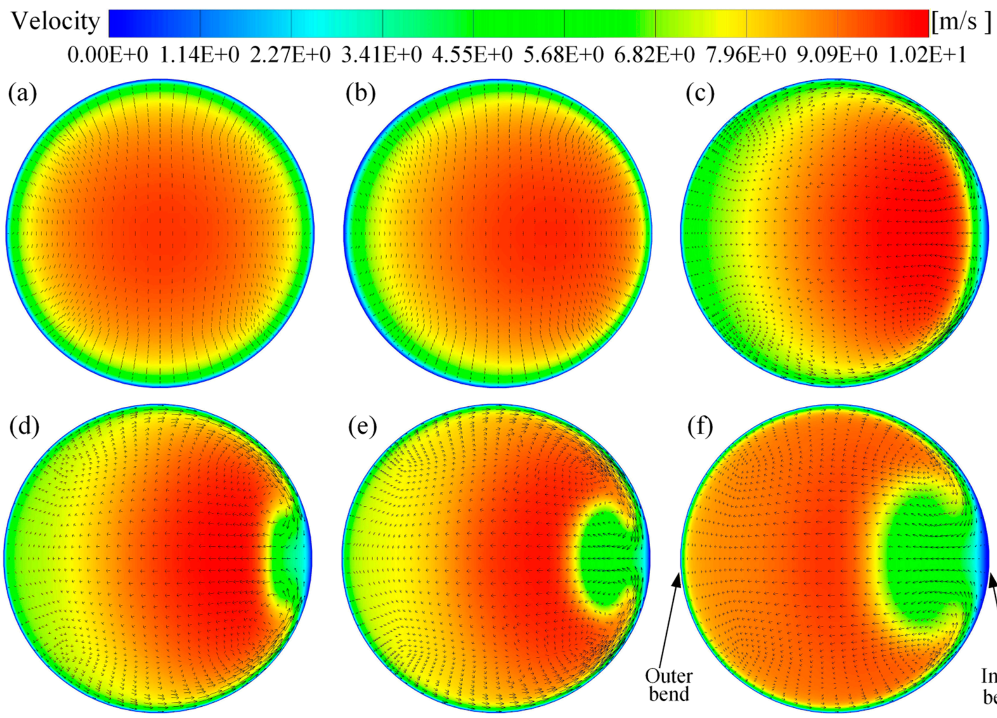

Figure 6. Comparison of velocity distribution at different cross-sections with $\delta = 2.0$: (**a**) cross-section with $\Delta Z/D = 1$; (**b**) 0° cross-section; (**c**) 30° cross-section; (**d**) 45° cross-section; (**e**) 60° cross-section; (**f**) 90° cross-section.

Upon entering the bend section, the flow structure is markedly altered by centrifugal forces and the resulting radial pressure gradient. In the initial segment of the bend (α = 0–30°), the high-velocity core region shifts progressively toward the inner wall, inducing a localized acceleration zone adjacent to it. As the flow develops, centrifugal effects increasingly drive fluid toward the outer wall. At α = 45°, a pronounced low-velocity region emerges near the inner wall, giving rise to a recirculation zone that extends from the inner to the outer wall. This recirculating vortex continues to strengthen as the flow develops downstream.

The vorticity distribution in the bend region is shown in Figure 7, where $|\omega^n|$ represents the vorticity intensity along the mainstream direction within the cross-section. A pair of Dean vortices exists, symmetrically distributed along the central axis A-A′ and rotating in opposite directions. This structure arises from centrifugal forces that drive the near-wall fluid towards the outer wall, thereby generating a radial pressure gradient within the cross-section and inducing a recirculation of the outer wall fluid towards the inner wall.

This is a typical feature of flow in bends, and its intensity is typically quantified using the Dean number (*De*).

$$De = Re\sqrt{D/2R_b}. \tag{33}$$

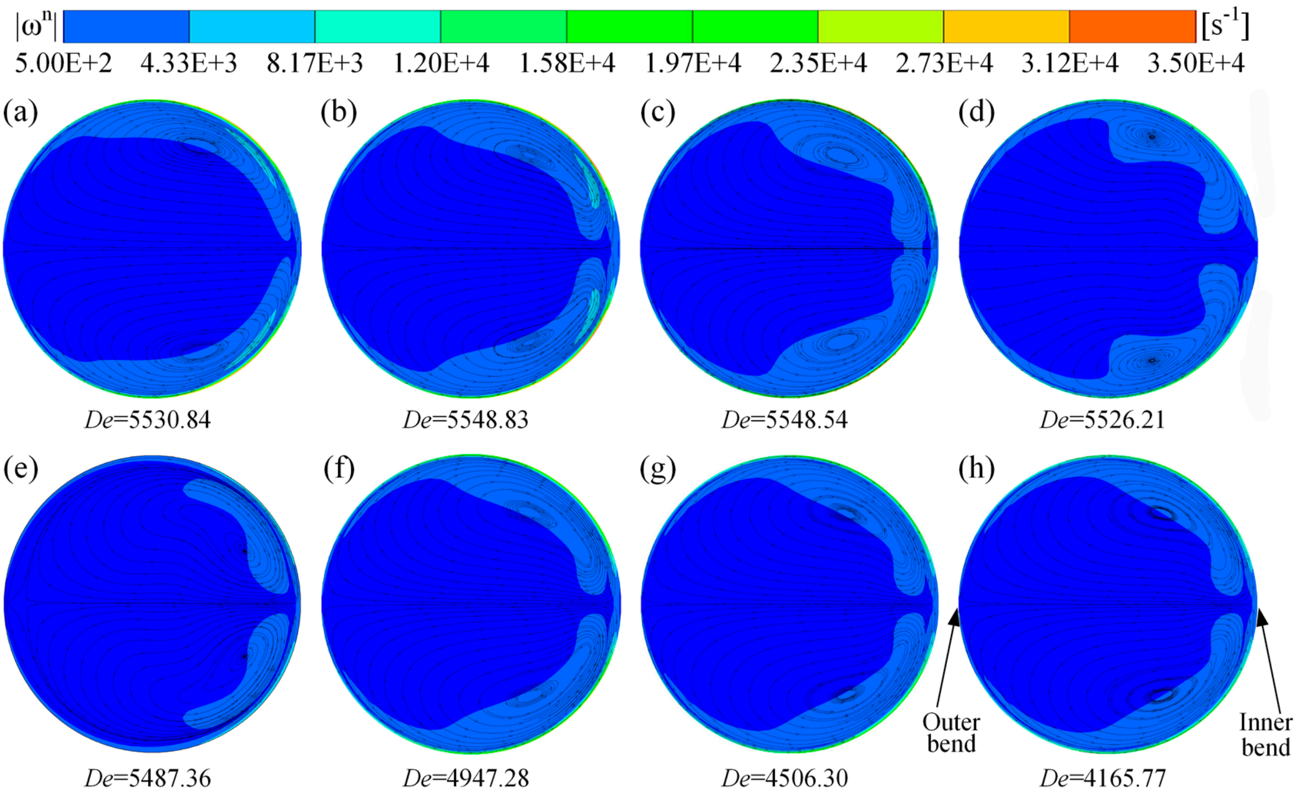

Figure 7. The vorticity field distribution in the bend region. (**a**–**e**): cross-sections at 30°, 45°, 60°, 90° and $\Delta X/D$ = 1 (δ = 2.0); (**f**–**h**): δ = 2.5, 3.0 and 3.5 (45° cross-section).

The vorticity is concentrated within the shear layer between the inner wall of the bend and the Dean vortex core. As the flow develops, the vorticity intensity first increases and then decreases. When α = 45°, the centrifugal force and viscous dissipation are in optimal balance, and the secondary flow intensity reaches the peak. Subsequently, viscous effects become dominant, causing a gradual decrease in the proportion of high-vorticity regions. This trend is consistent with the Dean vortex's variation along the flow direction. Notably, the Dean vortex structure is clearly observed in the downstream straight pipe at $\Delta X/D = 1$, indicating that the secondary flow exhibits significant persistence downstream, and its vorticity attenuation mainly depends on viscous diffusion.

To further clarify the evolution of secondary flow, the absolute vorticity flux (J^n_{ABS}) and the secondary flow Reynolds number (*Se*) are introduced for analysis [46]. As shown in Figure 8a, J^n_{ABS} and *Se* exhibit a trend of first increasing and then decreasing with flow development, reaching a peak at α = 45°, which is consistent with the variation pattern of the Dean vortex intensity. With the increase in δ, J^n_{ABS} and *Se* continue to decline. When combined with Figure 7b,f–h, it can be observed that the Dean vortex intensity weakens simultaneously, indicating that increasing δ reduces the centrifugal driving force, inhibits the momentum exchange between the mainstream region and the near-wall region, and thus weakens the development of secondary flow.

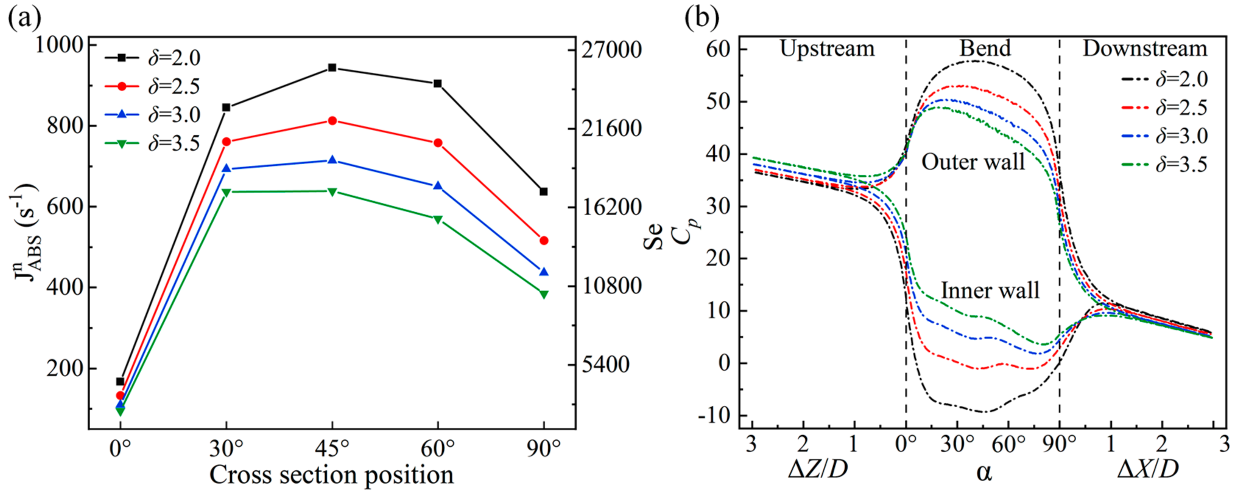

Figure 8. (**a**) The variation of J^n_{ABS} and Se with cross-sectional position under different δ conditions; (**b**) Pressure coefficient (C_p) along the inner and outer walls of the pipe under different δ conditions.

Further analysis indicates that changes in secondary flow intensity are closely related to the radial pressure gradient. As shown in Figure 8b, an increase in δ reduces the disparity between the pressure coefficients (C_p) of the inner and outer walls, accompanied by a decline in the radial pressure gradient. This gradient reaches its maximum at α = 45°, corresponding to the peak position of secondary flow intensity.

$$J^n_{ABS} = \frac{1}{A}\iint_0^A |\omega^n| dA, \tag{34}$$

$$Se = \frac{\rho(D \cdot J^n_{ABS})D}{\mu} = \frac{\rho D^2}{\mu} J^n_{ABS}. \tag{35}$$

In summary, the curvature ratio dominates the evolution of the Dean vortex structure by regulating the interaction between centrifugal force and the radial pressure gradient. Centrifugal force directs fluid from the inner wall toward the outer wall, while the radial pressure gradient drives high-pressure fluid back from the outer wall to the inner wall. Increasing δ inhibits this mechanism: on the one hand, the centrifugal force weakens, and the initial kinetic energy required for flow instability decreases accordingly; on the other hand, the Dean vortex's recovery ability decreases as the radial pressure gradient decreases. Ultimately, this reduces secondary flow intensity and the mixing efficiency of fluids in the core and near-wall regions, significantly impacting particle transport behavior in the bend pipe.

4.2. Particle Flow Distribution Characteristics

The particle flow distribution within the bend region exhibits significant differences, as shown in Figure 9. The low-inertia small particles (d_p = 3 μm, St = 0.041) primarily follow the fluid flow, exhibiting a "high-dispersion, weak-aggregation" pattern. When α ≥ 45°, the synergistic effects of Saffman lift force, Brownian motion, and turbulent diffusion lead to the gradual accumulation of particles in the low-velocity region near the inner wall, forming a T-shaped accumulation zone. As α further increases, this zone gradually migrates toward the center of the pipe, consistent with the observations reported by Noorani et al. [47].

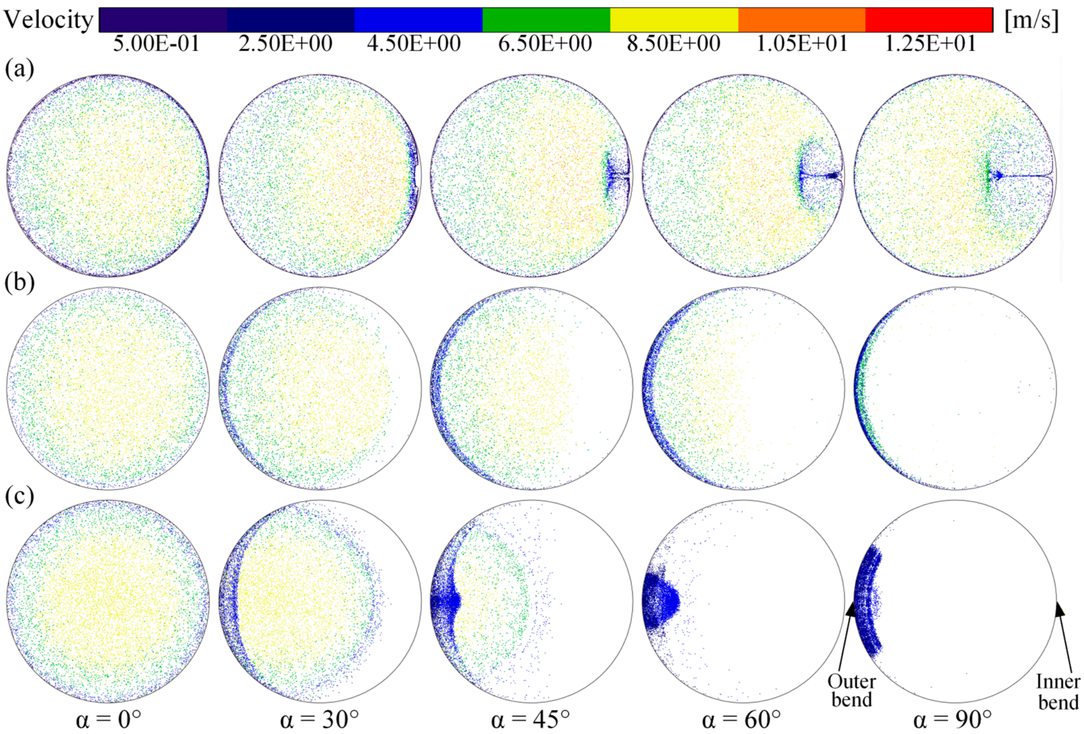

Figure 9. Particle flow distribution and velocity mapping in different cross-sections of the bend region (δ = 2.0): (**a**) 3 µm particles; (**b**) 18 µm particles; (**c**) 65 µm particles.

For low-inertia particles, the formation of the T-shaped low-velocity accumulation zone is the result of the synergistic interaction of multiple transport mechanisms. Specifically, in regions characterized by high velocity gradients, the Saffman lift force exerts a dominant influence on the particle lateral migration, thereby driving the particle accumulation toward the low-velocity regions. The random diffusion effect of Brownian motion leads to a diffused boundary of the particle accumulation zone, resulting in "blurred" edge characteristics. Turbulent diffusion dominates particle mixing in the mainstream region, thereby inhibiting excessive aggregation. In comparison, the Dean vortices exhibit limited efficiency in directionally transporting low-inertia particles, primarily guiding particles from the outer wall region toward the central region, thereby providing a macroscopic flow field framework for the final morphology of the T-shaped zone.

The motion behavior of particles with medium-inertia (d_p = 18 µm, St = 1.412) and high-inertia (d_p = 65 µm, St = 18.288) is dominated by inertial effects. The particles exhibit an "outer-wall agglomeration, inner-wall cavity" distribution pattern within the bend region. At α = 30°, a distinct low-velocity accumulation zone emerges near the outer wall, while a particle-sparse cavity forms near the inner wall. As α increases, the outer-wall accumulation intensifies, and the inner-wall cavity expands further. At α = 90°, particles adhere tightly on the outer wall, forming an extremely narrow rope-like accumulation zone, with velocities only 6.77–27.50% of the local gas velocity. This distribution pattern is closely related to the response ability of particles to fluid vortex structures. For particles with $St > 1$, the relaxation time is longer, and inertial effects are significant. Under the influence of strong centrifugal forces, particles cross the vortex core and migrate towards the outer wall, gradually accumulating there. Due to the lack of an effective particle replenishment mechanism, a persistent sparse region forms on the inner wall.

The flow distribution patterns of different inertia particles in pipes with varying δ are shown in Figure 10. The results indicate that the particle flow distribution in the bend region is jointly regulated by δ and particle inertia. For low-inertia particles, with the increase in δ, the centrifugal force, radial pressure gradient, and secondary flow intensity decrease synchronously, resulting in a reduction in the T-shaped accumulation zone on the inner wall side. However, within the non-aggregation zone, the particles continue to maintain a relatively uniform distribution.

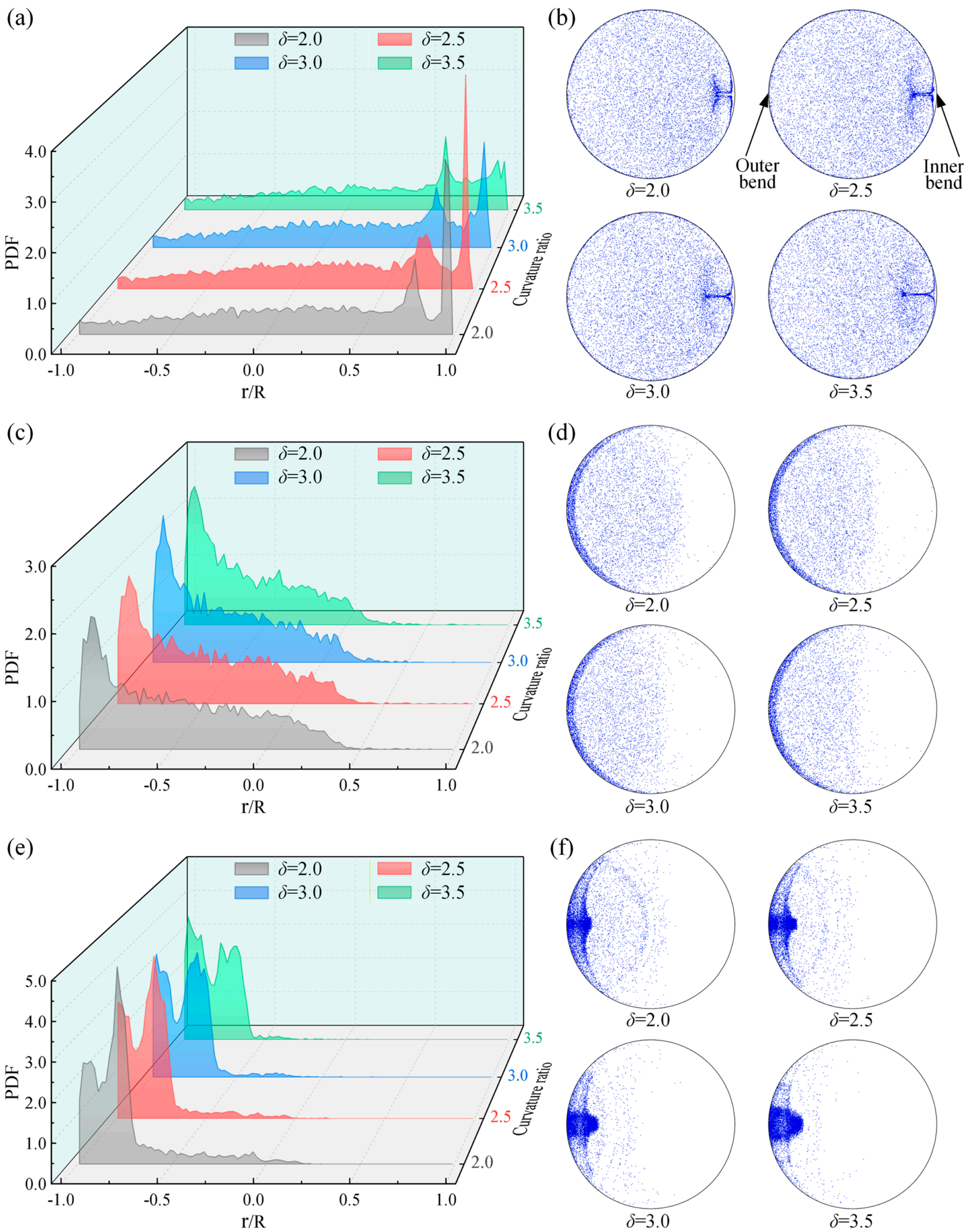

Figure 10. Particle distribution in the 45° cross-section at different δ conditions: (**a**,**b**) 3 µm particles; (**c**,**d**) 18 µm particles; (**e**,**f**) 65 µm particles; (**a**,**c**,**e**) Probability density function (PDF) distribution of particles along the centerline direction; (**b**,**d**,**f**) Particle position distribution in the cross-section.

The motion distribution of medium-inertia particles is jointly regulated by centrifugal force and secondary flow. Increasing δ enhances the relative contribution of centrifugal force to particle transport, which promotes further migration of particles to the outer wall, resulting in an increase in the probability density function (PDF) peak at the outer wall side. However, the increase in the cavity region on the inner wall side is limited, indicating that increasing δ does not have a significant effect on the dominant transport mechanism of medium-inertia particles.

The motion of high-inertia particles is primarily influenced by inertial and centrifugal forces [48]. Due to the long relaxation time of particles and the poor following ability of the Dean Vortex. It is difficult for them to be transported to the inner wall region by secondary flows [49]. Under the influence of centrifugal forces, the particles continuously migrate toward the outer wall, and their trajectories are hardly affected when crossing the vortex core. At the same time, the particles respond weakly to turbulent fluctuations near the outer wall and exhibit very limited transverse diffusion. These factors lead to the formation of a rope-like accumulation zone on the outer wall and an extensive cavity with PDF = 0 on the inner wall. As δ increases, the width of the accumulation zone on the outer wall increases, and its morphology expands from "rope-like" to "elliptical", while the range of the inner wall cavity expands further. The quantitative data on the velocity distribution of high-inertia particles within the full cross-section and its variation with curvature ratios are provided in Appendix A.

4.3. Particle Deposition Distribution Characteristics

Based on the differences in particle motion characteristics with distinct inertia, particles are divided into two states: the diffusion-inertia transition regime ($St < 1$) and the inertial collision-dominated regime ($St > 1$). In the diffusion-inertia transition regime, V_d^+ increases with St and reaches a peak near $St \approx 1$. In the inertial collision-dominated regime, V_d^+ decreases approximately linearly with increasing St, as shown in Figure 11a.

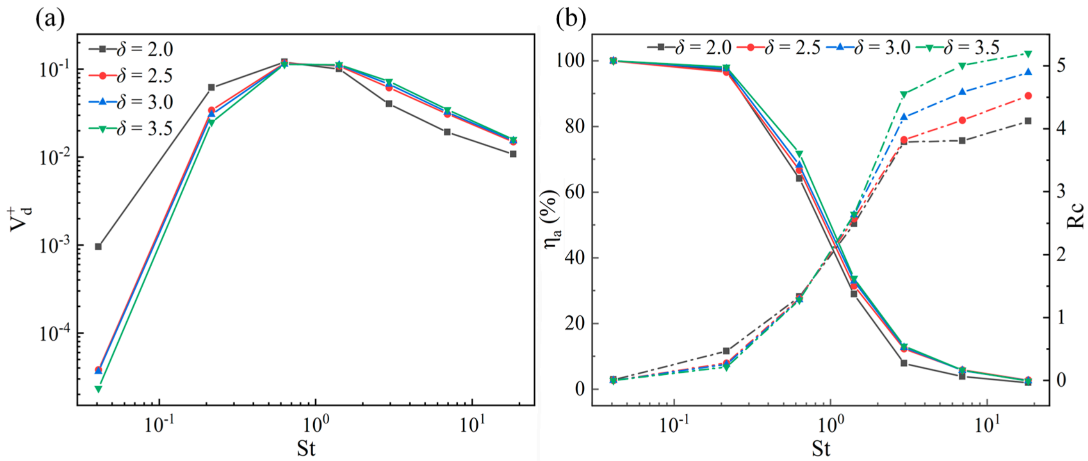

Figure 11. (**a**) Stokes number (St) and dimensionless deposition velocity (V_d^+); (**b**) Stokes number (St) and the effective collision coefficient Rc (dashed line) and the effective adhesion rate η_a (solid line).

Particle deposition can be divided into two stages: contact and adhesion, characterized by the effective collision coefficient (Rc) and the effective adhesion rate (η_a), respectively. Deposition occurs exclusively when a particle makes effective contact with the wall, and the probability of successful deposition subsequent to contact is contingent on adhesion probability. Consequently, V_d^+ can be regarded as the coupled result of Rc and η_a.

As shown in Figure 11b, for low-inertia particles ($St < 1$), $\eta_a \approx 100\%$. This indicates that particles can adhere when they contact with the wall. However, Rc is extremely low, which limits the occurrence of effective contact events. Consequently, particle deposition is governed by the contact stage, resulting in a low V_d^+. As St increases, Rc rises significantly, indicating a higher frequency of particle–wall collisions. Meanwhile, η_a decreases sharply, reflecting a reduction in adhesion efficiency. At $St \approx 1$, both Rc and η_a reach moderate levels, thereby establishing an optimal synergistic relationship. The relatively high contact frequency affords ample opportunities for adhesion, while the adhesion probability maintains a sufficiently high level, causing V_d^+ to reach its peak. When $St > 1$, the sustained decrease in η_a will restrict deposition, and the rebound effects will gradually dominate particle–wall interactions. Although Rc remains a high level, particles are more likely to rebound upon contact, making effective deposition difficult and causing V_d^+ to decrease steadily. These results indicate that particle deposition behavior is governed by the competitive interplay between the contact and adhesion stages. Specifically, low-inertia particles are limited by Rc, while high-inertia particles are constrained by η_a, with an optimal coupling achieved at $St \approx 1$.

To verify the universality of the δ in regulating the deposition behavior of particles with various inertia, two additional operating conditions were added: weak turbulence (Re = 5489.20) and strong turbulence (Re = 16,454.69). The three operating conditions (the original flow conditions: Re = 10,969.26) collectively form a comparative analysis of three distinct flow states. The particle deposition characteristics in pipes with different δ values were quantified by the dimensionless deposition velocity ratio (γ).

$$\gamma = \frac{V^+_{d,\delta\,=\,2.5\sim3.5}}{V^+_{d,\delta\,=\,2.0}}. \quad (36)$$

As shown in Figure 12, the regulatory effect of δ on particle deposition behavior exhibits a consistent trend across three turbulent conditions. Within the diffusion-inertia transition regime, increasing δ inhibits particle deposition ($\gamma < 1$), and the degree of inhibition increases with δ. There is a notable correlation between this deposition inhibition effect and the attenuation of secondary flow intensity induced by increasing δ. The weakening of the secondary flow reduces the lateral migration capability of particles, making low-inertia particles more susceptible to being carried out of the pipe by the mainstream, thereby inhibiting particle deposition. Conversely, in the inertial collision-dominated regime, increasing δ promotes deposition ($\gamma > 1$), and the degree of promotion also increases with δ. This is attributed to the motion of high-inertia particles, which is primarily governed by centrifugal forces. An increase in δ increases the curvature radius and prolongs the migration path of particles within the bend region. This enhances the probability of effective collisions with the pipe wall, thereby promoting deposition.

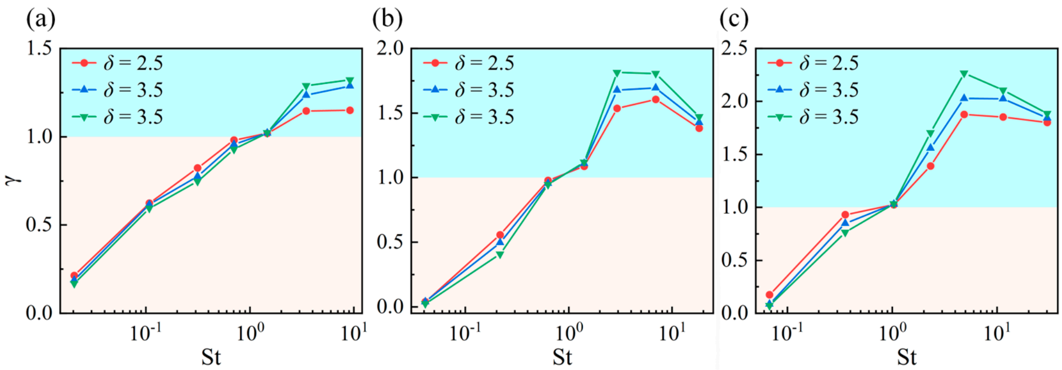

Figure 12. The relationship between the dimensionless deposition velocity ratio (γ) and Stokes number (St) under different flow conditions: (**a**) Re = 5489.20; (**b**) Re = 10,969.26; (**c**) Re = 16,454.69.

To investigate the spatial distribution characteristics of deposited particles, the pipe was divided into four distinct regions along the flow direction: R1 (Z: −200 to −100 mm), R2 (Z: −100 to 0 mm), R3 (0° to 90°), and R4 (X: 0 to 100 mm), as shown in Figure 13. The analysis compared the overall deposition distribution of seven characteristic particle sizes at different δ conditions, along with the turbulence intensity (It) on the ZX symmetry plane.

Total particle deposition increased by 7.91%, 14.26%, and 19.14% as δ increased from 2.5 to 3.5. This growth trend is closely associated with changes in flow field structure and particle dynamics: increasing δ significantly weakens the radial pressure gradient and secondary flow intensity, thereby inhibiting the evolution of turbulent energy, as reflected by the reduced turbulent intensity in the figure. This attenuation effectively reduces the entrainment and resuspension of particles by turbulent vortices, creating favorable conditions for particle deposition.

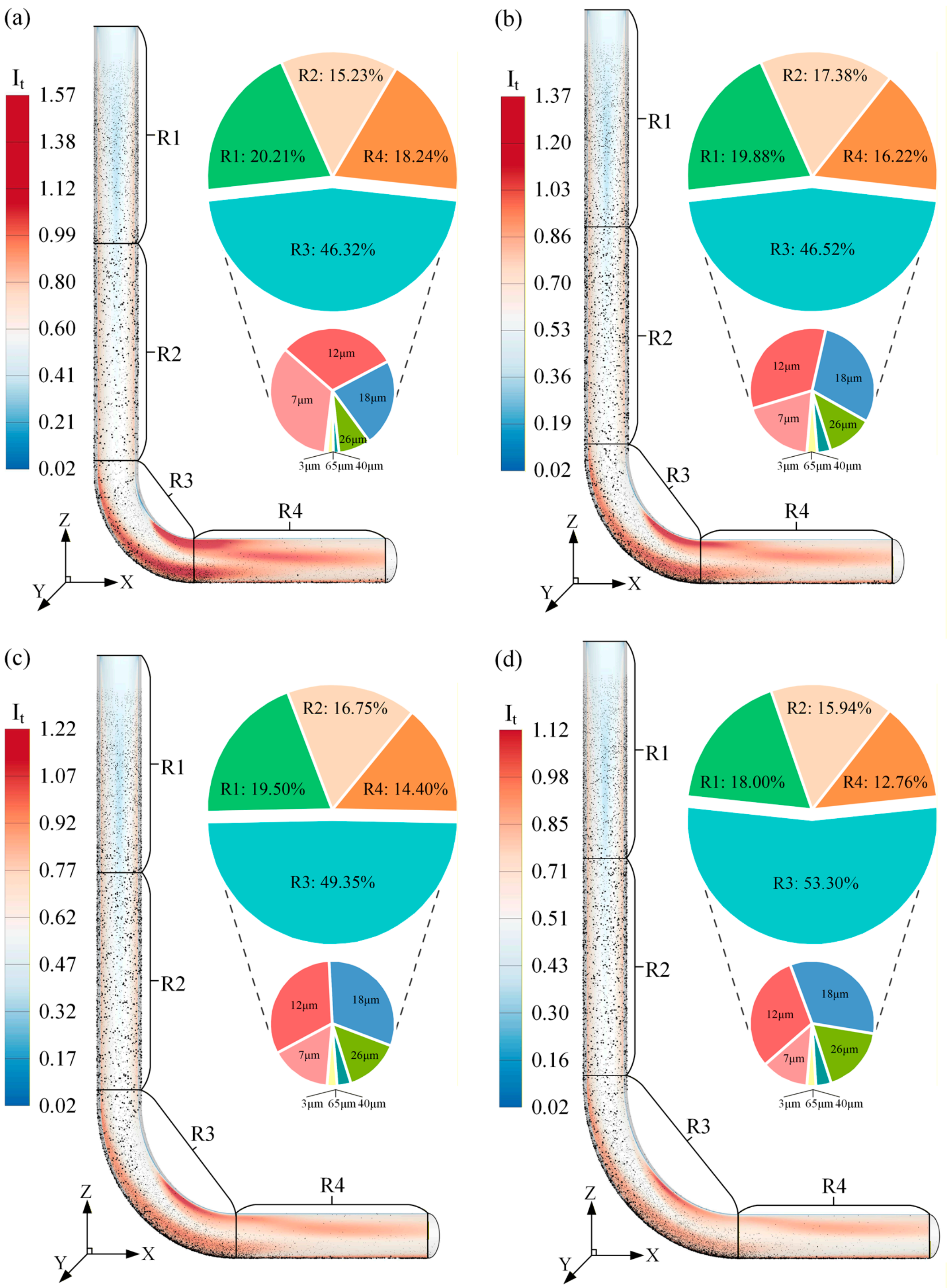

Figure 13. The overall deposition distribution of seven characteristic particle sizes and turbulence intensity on the ZX symmetry plane at different δ: (**a**) δ = 2.0; (**b**) δ = 2.5; (**c**) δ = 3.0; (**d**) δ = 3.5.

From the perspective of particle dynamics, the deposition behavior exhibits distinct responses in different *St* states. In the inertial collision-dominated regime ($St > 1$), particles possess high inertia, and their trajectories are less affected by flow fluctuations. An increase in δ results in more gradual streamline curvature, reducing the impact angle (θ) when particles impact the wall. This reduction lowers the normal restitution coefficient and enhances kinetic energy dissipation during collision, thereby effectively inhibiting particle rebound. This mechanism predominates in the inertial collision-dominated regime ($St > 1$), where the resulting gain in deposition substantially outweighs the deposition inhibition observed in the diffusion-inertial transition regime ($St < 1$), emerging as the primary factor driving the overall increase in deposition.

Notably, as δ increases, the number of deposited particles also rises in the upstream R2 region. This phenomenon results from the "pre-bend flow field" effect, which intensifies and extends upstream near the entrance of the R3 region. Before the fluid enters the core curved section (R3), streamlines begin to deflect in advance due to the influence of the downstream bend curvature [50]. With increasing δ, the initiation point of this streamline deflection extends further upstream to accommodate the larger curvature radius, causing the flow field in the R2 region to exhibit bending characteristics earlier. This extended streamline curvature significantly increases the probability of particle collisions with the pipe wall before entering the core bend region, thereby enhancing deposition in the R2 region.

Furthermore, the deposition contribution of each region is quantified by defining the regional relative deposition rate (η_r), where $N_{d,i}$ denotes the number of particles deposited in region *i*.

$$\eta_r = \frac{N_{d,i}}{N_{dep}} \times 100\%. \quad (37)$$

In regions R1 and R2, η_r gradually decreases along the flow direction, with particles exhibiting a uniform radial distribution. Upon entering the R3, the synergistic effects of strong inertial effects and centrifugal forces significantly increase particle collisions with the outer wall of the bend, causing η_r to reach its maximum. This confirms that R3 is the primary deposition zone. Within this region, the high-inertia particles accumulate toward the outer wall at the dominance of centrifugal forces, resulting in a structure where high-inertia particles accumulate on the outer wall while low-inertia particles disperse along the inner wall. This further exacerbates the radial deposition gradient in R3 region. As δ increases, the reduction in turbulent intensity weakens the entrainment capacity of the fluid, raising η_r in R3 from 46.23% to 53.30%. In the R4 region, curvature effects disappear, and both secondary flow and turbulence intensity decrease substantially. Driven persistently by inertial effects, particles primarily contact the pipe bottom, significantly reducing the effective deposition area and leading to a rapid decline in η_r.

5. Conclusions

In this study, a coupled numerical method of RSM and DPM was employed, combined with a UDF to construct a particle-wall interaction model. The motion characteristics and deposition distribution of sepiolite particles with diameters from 1 to 100 μm, were systematically analyzed in a 90° bend pipe within a pneumatic conveying system. The simulation covered the following conditions: pipe curvature ratio δ = 2.0–3.5, Reynolds number Re = 5489.20–16,454.69, and particle Stokes number St = 0.020–30.176. The main conclusions are as follows:

1. The dynamic behavior of particles in the bend is synergistically regulated by the inertial effect and the secondary flow:

The low-inertia particles exhibit a "high-dispersion, weak-aggregation" distribution pattern. The high-inertia particles exhibit an "outer-wall agglomeration, inner-wall cavity" distribution pattern. The transition between these patterns occurs near $St \approx 1$, indicating that the dominant mechanism of particle transport changes from turbulent diffusion to inertial transport.

2. The curvature ratio exhibits a non-monotonic regulatory effect on the deposition of particles with different inertia:

In the diffusion-inertial transition regime ($St < 1$), increasing the curvature ratio inhibits particle deposition, and the degree of inhibition increases with the curvature ratio. The observed deposition inhibition effect correlates well with the attenuation of secondary flow intensity caused by the increase in curvature ratio. In the inertial collision-dominated regime ($St > 1$), increasing the curvature ratio enhances the probability of effective collisions between particles and the pipe wall. Consequently, particle deposition is promoted, and the extent of this promotion increases with curvature ratio.

3. The sensitivity of particle deposition distribution to curvature changes stems mainly from the inertial-screening effect in the near-wall region:

Increasing δ not only attenuates secondary flow and turbulence intensity, reducing the resuspension effect of fluid on particles, but also enhances the inertial screening effect in R3 region. This combination raises the deposition density gradient on the outer wall and expands the cavity zone on the inner wall, thereby enabling effective regulation of particle deposition patterns.

The present study focuses on the typical structure of a 90° bend pipe. Although the model is representative, the actual pneumatic conveying system includes complex geometric structures, such as different angles (45°, 60°, and 135°) and rectangular bends. Moreover, the curvature ratio studied covers the typical range from sharp to gentle bends, but does not involve the flow and deposition characteristics in pipes with a large curvature ratio ($\delta > 4$), which may limit the generalizability of the research conclusions.

In future research, consideration could be given to broadening the range of geometric configurations and operating conditions, and further expanding the research scope of bend angles and curvature ratios. It is essential to investigate the critical conditions for the secondary flow structure instability and particle deposition mode transition under extreme operating conditions.

Author Contributions: Conceptualization, T.G. and Y.Z.; methodology, T.G.; software, T.G.; validation, T.G.; formal analysis, X.T. and Y.X.; investigation, T.G.; resources, Y.Z.; data curation, T.G.; writing—original draft preparation, T.G.; writing—review and editing, T.G.; visualization, T.G.; supervision, X.T., Z.L., D.L. and Y.X.; project administration, T.G. and Y.Z.; funding acquisition, T.G., Y.Z., Z.L. and D.L. All authors have read and agreed to the published version of the manuscript.

Funding: This research was funded by the National Natural Science Foundation of China (52175254); Hunan Provincial Innovation Foundation for Postgraduate (CX20230550, CX20240614, XDCX2025Y297, XDCX2025Y301).

Data Availability Statement: The original contributions presented in this study are included in the article. Further inquiries can be directed to the corresponding authors.

Conflicts of Interest: The authors declare no conflicts of interest.

Abbreviations

The following abbreviations are used in this manuscript:

A	Cross sectional area (m^2)
C_c	Cunningham correction factor
C_D	Particle drag coefficient
C_p	Pressure coefficient
D	Pipe inner diameter (m)
De	Dean number
d_p	Particle diameter (m)
E	Effective stiffness (N/m)
$\overline{E}_k$	Mean kinetic energy
$E_{k,in}$	Kinetic energy of inlet particles
$\overline{E}_k^*$	Dimensionless mean kinetic energy
$E_s,\ E_p$	Equivalent Young's modulus of wall and particle (Pa)
e_n, e_t	Normal and tangential restitution coefficients
F_B	Brownian force (m/s^2)
F_D	Drag force (N)
F_S	Saffman lift force (m/s^2)
f_{low}	Proportion of low-kinetic particles
g	Gravity acceleration (m/s^2)
H	Inlet section length (m)
I_t	Turbulence intensity
J_{ABS}^n	Absolute vorticity flux (s^{-1})
K	Composite Young's modulus (Pa)
k	Turbulent energy (m^2/s^2)
L	Outlet section length (m)
Lc	Computational domain length (m)
m_p	Particle mass (kg)
N_c	Contact frequency
N_{dep}	Number of deposited particles
$N_{d,i}$	Number of deposited particles in region i
N_{dn}	Total deposition of specific sized particles
$N_{dn,i}$	Total deposition of specific sized particles in region i
N_{in}	Number of releaseed particles
P_{state}	Contact state
R	Particle restitution coefficient
R_b	Curvature radius (m)
R_c	Effective collision coefficient
Re	Flow Reynolds number
Re_p	Particle Reynolds number
Re_y	Wall Reynolds number
r_i, r_o	Radius of inner and outer walls of bends (m)
r^*	Dimensionless wall distance
S	Particle fluid density ratio
Se	Secondary flow Reynolds number
S_{ij}	Mean strain-rate tensor (s^{-1})
St	Stokes number
T_L	Integral time scale
u	Air velocity (m/s)
u_i'	Fluctuation velocity (m/s)
u_m	Air mean velocity (m/s)
u_p	Particle velocity (m/s)
u_s	Streamwise velocity (m/s)
u^*	Wall frictional velocity (m/s)
v_{cr}	Critical deposition velocity (m/s)
v_{pn}, v_{pt}	Normal and tangential impact velocity of particle (m/s)
$v_{\tau,crit}$	Critical shear velocity (m/s)
V_d	Particle deposition velocity (m/s)
V_d^+	Dimensionless deposition velocity
W_A	Adhesion work (J/m^2)
y	Normal distance of the wall (m)
Abbreviations	
DPM	Discrete phase model
DRW	Discrete random walk model
EWT	Enhanced wall treatment
PDF	Probability density function
RSM	Reynolds stress model
UDF	User-Defined Function
Greek symbols	
α	Bend deflection angle (°)
γ	Dimensionless deposition velocity ratio
δ	Curvature ratio
ε	Turbulent dissipation rate (m^2/s^3)
ζ	Normally distributed random number
η_a	Effective adhesion rate (%)
η_r	Regional relative deposition rate (%)
θ	Impact angle (°)
l_μ, l_ε	Turbulence length scales (m)
k_b	Boltzmann constant
λ	Gas molecule free path (m)
μ	Dynamic viscosity (kg/m·s)
ν_s, ν_p	Poisson's ratio of wall and particle
ρ	Air density (kg/m^3)
ρ_p	Particle density (kg/m^3)
τ_e	Turbulent eddy time scale (s)
τ_p	Particle relaxation time (s)
τ_s	System response time (s)
τ_w	Wall shear stress (Pa)
$\tau_{w,crit}$	Critical wall shear stress (Pa)
v	kinematic viscosity (m^2/s)
v_t	Eddy viscosity (m^2/s)
ω^n	Vorticity intensity in mainstream direction (s^{-1})

Appendix A

The velocity distribution of high-inertia particles across the cross-section of the bend region under varying δ conditions is shown in Figure A1. The overall particle velocity distribution gradually decreases as α increases. This trend is further quantified by the velocity frequency distribution of high-inertia particles, as depicted in Figure A2. As α increases, the peak value in the high-velocity region gradually decreases, while that in the low-velocity region gradually increases, with the velocity peak gradually shifting towards the low-velocity region. After α = 45°, the principal velocity peak is situated within the low-velocity region, and the distribution becomes more extensive. This suggests that particle collisions become increasingly random, with multiple collisions significantly attenuating particle velocity.

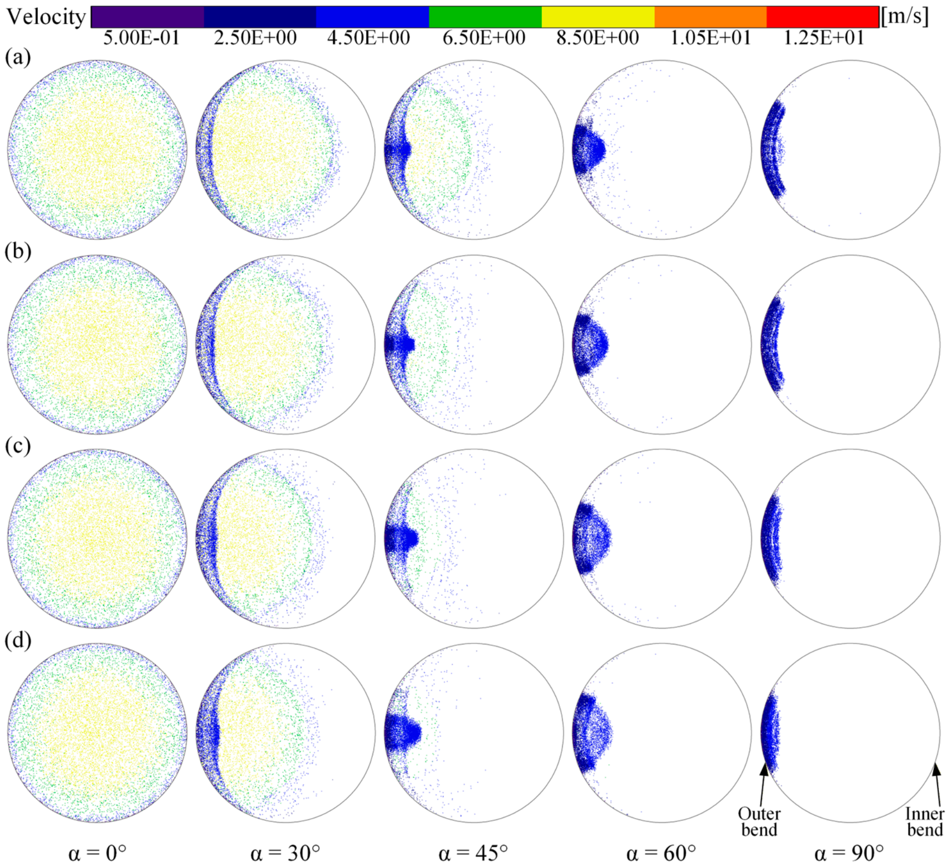

Figure A1. Particle flow distribution and velocity mapping within different cross-sections in the bend region (65 μm particles): (**a**) δ = 2.0; (**b**) δ = 2.5; (**c**) δ = 3.0; (**d**) δ = 3.5.

The distribution of particle kinetic energy across various δ pipe cross-sections was analyzed using the dimensionless mean kinetic energy ($\overline{E}_k^*$), as shown in Figure A3a. On the cross-section of α = 90°, $\overline{E}_k^*$ increases from 0.2797 when δ = 2.0 to 0.3515 when δ = 3.5. Correspondingly, the kinetic energy loss rate ($1 - \overline{E}_k^*$) exhibits a decline from 72.03% to 64.84%, indicating that collisions on the inner wall of small δ pipes result in more significant kinetic energy dissipation.

$$\overline{E}_k^* = \frac{\overline{E}_k}{E_{k,in}}, \tag{A1}$$

$$\overline{E}_k(\alpha, \delta) = \frac{1}{N}\sum_{i=1}^{N}\frac{1}{2}m_p \mid \vec{u}_{p,i} \mid^2 . \tag{A2}$$

where $\overline{E}_k$ is the mean kinetic energy of the particles within the cross section, and $E_{k,in}$ is the kinetic energy of the inlet particles.

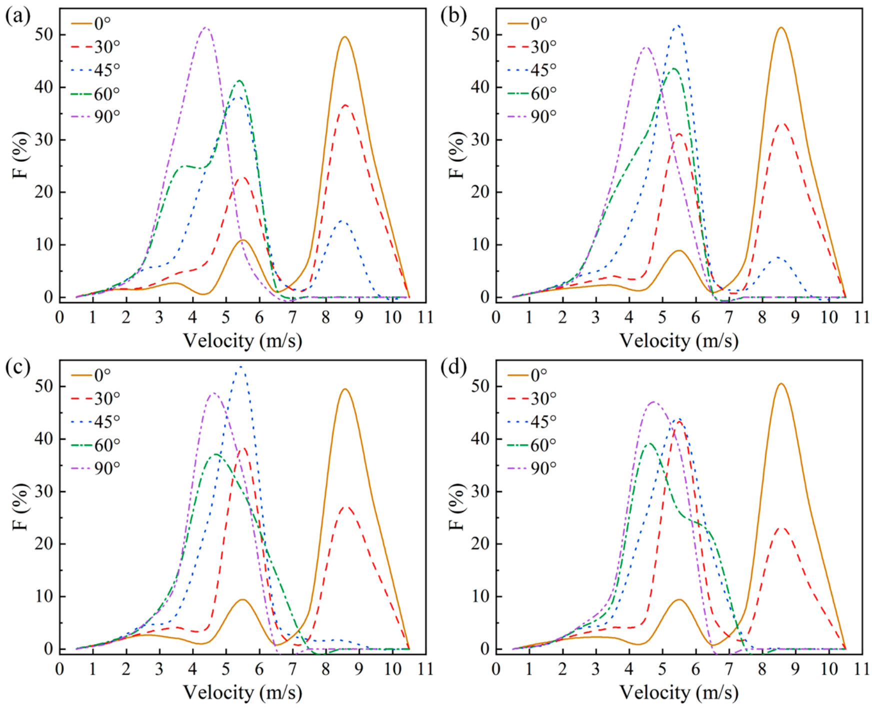

Figure A2. The velocity frequency distribution of high-inertia particles: (**a**) δ = 2.0; (**b**) δ = 2.5; (**c**) δ = 3.0; (**d**) δ = 3.5.

A noteworthy phenomenon is observed at the cross-sections of α = 30° and 45°, where $\overline{E}_k^*$ decreases with the increase in δ. As illustrated in Figure A2, as δ increases, the high-velocity peak gradually decreases, and the low-velocity peak gradually increases at α = 30° and 45°. This indicates that particles in pipes with large δ will experience collisions earlier or more frequently, leading to a faster loss of kinetic energy during the initial stage of particle flow in the bend region. This finding suggests that the duration and intensity of particle-wall interactions are not monotonically regulated by δ, but rather depend on the flow's developmental stage.

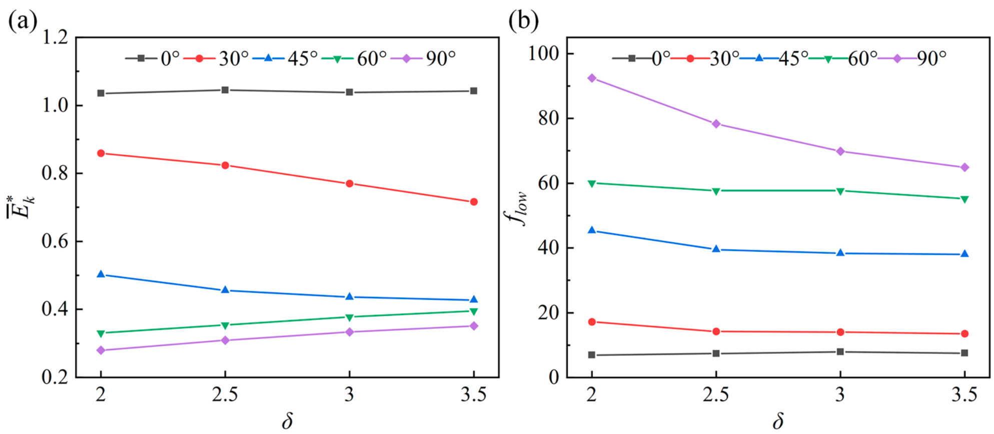

Figure A3. (**a**) The variation in dimensionless mean kinetic energy of particles $\overline{E}_k^*$ with δ; (**b**) The variation in the proportion of low-kinetic particles f_{low} with δ.

$$f_{low}(\alpha) = \frac{N(E_k < 0.4E_{k,in})}{N_{total}} \times 100\%. \tag{A3}$$

To further quantify the effect of wall collisions, the proportion of particles with kinetic energy below $0.4E_{k,in}$ is defined as the proportion of low-kinetic particles (f_{low}). As shown in Figure A3b, f_{low} decreases with the increase in δ, while increases with the increase in α. At $\alpha = 90°$, the f_{low} decreases from 92.48% when $\delta = 2.0$ to 64.93% when $\delta = 3.5$. This further demonstrates that small δ pipes experience more significant kinetic energy dissipation due to enhanced particle-wall interactions.

References

1. Klinzing, G.E. A review of pneumatic conveying status, advances and projections. *Powder Technol.* **2018**, *333*, 78–90. [CrossRef]
2. Setia, G.; Mallick, S.S.; Wypych, P.W. On improving solid friction factor modeling for fluidized dense-phase pneumatic conveying systems. *Powder Technol.* **2014**, *257*, 88–103. [CrossRef]
3. Jin, Y.; Gu, W. Stochastic analysis in gas–solid two-phase flow in the dense-phase pneumatic conveying of pulverized coal. *Chin. J. Chem. Eng.* **2025**, *83*, 26–37. [CrossRef]
4. Zhang, K.; Huang, L.; Nie, D. Cylindrical Microparticle Transport and Deposition from Electrokinetic Microflow in a 90 Degree Bend. *Math. Comput. Appl.* **2010**, *15*, 822–827. [CrossRef]
5. Huang, J.; Liu, G.; Fan, S.; Li, B.; Li, C. Numerical simulation of sulfur particle agglomeration at bends of high sulfur natural gas gathering pipelines based on Euler-PBM coupling. *Sci. Rep.* **2025**, *14*, 19190. [CrossRef]
6. Drescher, E.; Mohseni-Mofidi, S.; Bierwisch, C.; Kruggel-Emden, H. A numerical assessment of different geometries for reducing elbow erosion during pneumatic conveying. *Powder Technol.* **2025**, *449*, 120357. [CrossRef]
7. Zeng, D.; Zhang, E.; Ding, Y.; Yi, Y.; Xian, Q.; Yao, G.; Zhu, H.; Shi, T. Investigation of erosion behaviors of sulfur-particle-laden gas flow in an elbow via a CFD-DEM coupling method. *Powder Technol.* **2018**, *329*, 115–128. [CrossRef]
8. Ma, A.C.; Williams, K.C.; Zhou, J.M.; Jones, M.G. Numerical study on pressure prediction and its main influence factors in pneumatic conveyors. *Chem. Eng. Sci.* **2010**, *65*, 6247–6258. [CrossRef]
9. Yan, F.; Cheng, S.; Yang, Z.; Zhang, J.; Zhu, R. Pressure drop prediction in a pneumatic conveying system with different curvature radius pipes for conveying particles. *Part. Sci. Technol.* **2024**, *42*, 755–774. [CrossRef]
10. Sun, S.; Yuan, Z.; Peng, Z.; Moghtaderi, B.; Doroodchi, E. Computational investigation of particle flow characteristics in pressurised dense phase pneumatic conveying systems. *Powder Technol.* **2018**, *329*, 241–251. [CrossRef]
11. Yan, F.; Yang, Z.Y.; Tu, P.; Zhu, R. Particle Dynamic Characteristics of the Vertical Tubes in a Horizontal-Vertical Pneumatic Conveying System with Different Curvature Radius Bends. *J. Appl. Fluid Mech.* **2022**, *15*, 1759–1770. [CrossRef]
12. Benyamine, M.; Fezzioui, N.; Tehirichi, Z.; Alkhafaji, M.A.; Chambashi, G.; Kaid, N.; Menni, Y. Three-dimensional finite element analysis of turbulent crude oil flow and solid particle deposition patterns in circular curved pipelines. *AIP Adv.* **2024**, *14*, 105013. [CrossRef]
13. Shao, D.; Zhang, C.; Rao, Y.; Wang, S.; Li, F.; Yu, M.; Su, W.; Wu, W.; Gong, Z. Numerical Simulation Study on the Effect of Bend Angle on the Flow Characteristics of Natural Gas Hydrate Particles. *Energy Sci. Eng.* **2025**, *13*, 512–529. [CrossRef]
14. Eustice, J. Flow of Water in Curved Pipes. *Proc. R. Soc. Lond. Ser. A* **1910**, *84*, 107–118. [CrossRef]
15. Dean, W.R. LXXII. The stream-line motion of fluid in a curved pipe (Second paper). *Lond. Edinb. Dublin Philos. Mag. J. Sci.* **1928**, *5*, 673–695. [CrossRef]
16. Conté, I.; Peng, X.F. Numerical investigations of laminar flow in coiled pipes. *Appl. Therm. Eng.* **2008**, *28*, 423–432. [CrossRef]
17. Kim, J.; Yadav, M.; Kim, S. Characteristics of Secondary Flow Induced by 90-Degree Elbow in Turbulent Pipe Flow. *Eng. Appl. Comp. Fluid Mech.* **2014**, *8*, 229–239. [CrossRef]
18. Inthavong, K. A unifying correlation for laminar particle deposition in 90-degree pipe bends. *Powder Technol.* **2019**, *345*, 99–110. [CrossRef]
19. Lira, S.H.; Torres, M.J.; Silva, R.G.; Viñuela, J.Z. Numerical Characterization of the Solid Particle Accumulation in a Turbulent Flow through Curved Pipes by Means of Stokes Numbers. *Appl. Sci.* **2021**, *11*, 7381. [CrossRef]
20. Li, Q.; Song, J.; Li, C.; Wei, Y.; Chen, J. Numerical and experimental study of particle deposition on inner wall of 180° bend. *Powder Technol.* **2013**, *237*, 241–254. [CrossRef]
21. Sun, K.; Lu, L.; Jiang, H.; Jin, H. Experimental Study of Solid Particle Deposition in 90° Ventilated Bends of Rectangular Cross Section with Turbulent Flow. *Aerosol Sci. Tech.* **2013**, *47*, 115–124. [CrossRef]
22. Yan, Y.; Mortimer, L.F.; Wolde, B.; Fairweather, M.; Zhao, Y.; Yao, J. Effect of secondary flow and wall collisions on particle-laden flows in 90° pipe bends. *Int. J. Multiph. Flow* **2024**, *179*, 104925. [CrossRef]
23. Yang, Z.; Yan, F.; Tu, P.; Zhu, R. Experimental and numerical study of installing a dune model in a 90° bend in the horizontal-vertical pneumatic conveying system. *Particuology* **2023**, *79*, 14. [CrossRef]
24. Berrouk, A.S.; Laurence, D. Stochastic modelling of aerosol deposition for LES of 90° bend turbulent flow. *Int. J. Heat Fluid Flow* **2008**, *29*, 1010–1028. [CrossRef]
25. Jiang, H.; Lu, L.; Sun, K. Experimental study and numerical investigation of particle penetration and deposition in 90° bent ventilation ducts. *Build Environ.* **2011**, *46*, 2195–2202. [CrossRef]

26. Vasquez, E.S.; Walters, K.B.; Walters, D.K. Analysis of Particle Transport and Deposition of Micron-Sized Particles in a 90° Bend Using a Two-Fluid Eulerian–Eulerian Approach. *Aerosol Sci. Tech.* **2015**, *49*, 692–704. [CrossRef]
27. Guo, J.; Chen, Z.; Shen, B.; Wang, J.; Yang, L. Numerical study on characteristics of particle deposition efficiency on different walls of 90° square bend. *Powder Technol.* **2020**, *364*, 572–583. [CrossRef]
28. Wang, L.; Gao, D.; Zhang, Y. Numerical Simulation of Turbulent Flow of Hydraulic Oil through 90° Circular-sectional Bend. *Chin. J. Mech. Eng.* **2012**, *25*, 905–910. [CrossRef]
29. Tian, L.; Ahmadi, G. Particle deposition in turbulent duct flows—Comparisons of different model predictions. *J. Aerosol Sci.* **2007**, *38*, 377–397. [CrossRef]
30. Zhang, P.; Roberts, R.M.; Bénard, A. Computational guidelines and an empirical model for particle deposition in curved pipes using an Eulerian-Lagrangian approach. *J. Aerosol Sci.* **2012**, *53*, 1–20. [CrossRef]
31. Sun, K.; Lu, L.; Jiang, H. A computational investigation of particle distribution and deposition in a 90° bend incorporating a particle–wall model. *Build. Environ.* **2011**, *46*, 1251–1262. [CrossRef]
32. Wolfshtein, M. The velocity and temperature distribution in one-dimensional flow with turbulence augmentation and pressure gradient. *Int. J. Heat Mass Transf.* **1969**, *12*, 301–318. [CrossRef]
33. Hong, W.; Wang, X.; Zheng, J. Numerical study on particle deposition in rough channels with different structure parameters of rough elements. *Adv. Powder Technol.* **2018**, *29*, 2895–2903. [CrossRef]
34. Hongtao, L.; Li, Z. Prediction of particle deposition characteristic in 90° square bend: Square bend particle deposition characteristic. *Appl. Therm. Eng.* **2011**, *31*, 3402–3409. [CrossRef]
35. Brach, R.M.; Dunn, P.F. Macrodynamics of Microparticles. *Aerosol Sci. Tech.* **1995**, *23*, 51–71. [CrossRef]
36. Rong, W.; Feng, Y.; Schwarz, P.; Witt, P.; Li, B.; Song, T.; Zhou, J. Numerical study of the solid flow behavior in a rotating drum based on a multiphase CFD model accounting for solid frictional viscosity and wall friction. *Powder Technol.* **2020**, *361*, 12. [CrossRef]
37. Paz, C.; Suarez, E.; Eiris, A.; Porteiro, J. Development of a Predictive CFD Fouling Model for Diesel Engine Exhaust Gas Systems. *Heat Transf. Eng.* **2013**, *34*, 674–682. [CrossRef]
38. Soltani, M.; Ahmadi, G. On particle adhesion and removal mechanisms in turbulent flows. *J. Adhes. Sci. Technol.* **1994**, *8*, 763–785. [CrossRef]
39. Akermann, K.; Renze, P. Numerical study of turbulent heat transfer and particle deposition in enhanced pipes with helical roughness. *Int. J. Multiph. Flow* **2024**, *176*, 104827. [CrossRef]
40. Nilsen, K.M.; Kong, B.; Fox, R.O.; Hill, J.C.; Olsen, M.G. Effect of inlet conditions on the accuracy of large eddy simulations of a turbulent rectangular wake. *Chem. Eng. J.* **2014**, *250*, 175–189. [CrossRef]
41. Yan, Y.; Zhao, Y.; Yao, J.; Wang, C.H. Investigation of particle transport by a turbulent flow through a 90° bend pipe with electrostatic effects. *Powder Technol.* **2021**, *394*, 547–561. [CrossRef]
42. Lu, H.; Lu, L. A numerical study of particle deposition in ribbed duct flow with different rib shapes. *Build. Environ.* **2015**, *94*, 11. [CrossRef]
43. Wu, X.; Moin, P. A direct numerical simulation study on the mean velocity characteristics in turbulent pipe flow. *J. Fluid Mech.* **2008**, *608*, 81–112. [CrossRef]
44. Sudo, K.; Sumida, M.; Hibara, H. Experimental investigation on turbulent flow in a circular-sectioned 90-degree bend. *Exp. Fluids* **1998**, *25*, 42–49. [CrossRef]
45. Kliafas, Y.; Holt, M. LDV measurements of a turbulent air-solid two-phase flow in a 90° bend. *Exp. Fluids* **1987**, *5*, 73–85. [CrossRef]
46. Zhang, J.; Zhao, C.; Wang, L. Relationship between the Intensity of Secondary Flow and Convection Heat Transfer in a Helically Coiled Circular Tube with Uniform Wall Temperature. *J. Therm. Sci.* **2023**, *32*, 1007–1022. [CrossRef]
47. Noorani, A.; Sardina, G.; Brandt, L.; Schlatter, P. Particle transport in turbulent curved pipe flow. *J. Fluid Mech.* **2016**, *793*, 248–279. [CrossRef]
48. Harding, B.; Stokes, Y.M. Inertial focusing of non-neutrally buoyant spherical particles in curved microfluidic ducts. *J. Fluid Mech.* **2020**, *902*, A4. [CrossRef]
49. Clime, L.; Morton, K.J.; Hoa, X.D.; Veres, T. Twin tubular pinch effect in curving confined flows. *Sci. Rep.* **2015**, *5*, 9765. [CrossRef]
50. Zhao, Y.; Yan, Y.; Zhou, X.; Yao, J.; Wang, C.-H. Numerical investigation of electrostatic effect on particle behavior in a 90 degrees bend. *Adv. Powder Technol.* **2021**, *32*, 810–824. [CrossRef]

https://doi.org/10.3390/pr14081261